Modelling of friction and dilatancy effects at brittle interfaces for monotonic and cyclic loading

Stanisław Stupkiewicz and Zenon Mróz

Institute of Fundamental Technological Research, Polish Academy of Sciences

Świętokrzyska 21, 00-049 Warsaw, Poland

e-mail: sstupkie@ippt.gov.pl, zmroz@ippt.gov.pl

Abstract

The most important effects related to monotonic and cyclic response of contact interfaces of brittle materials are analyzed in the paper. Next, the available constitutive models are reviewed with respect to their ability to describe these effects. Several micro-mechanical mechanisms are analyzed including decohesion, interaction of primary and secondary asperities, asperity wear and damage and formation of a third body granular layer. Finally, we propose new formulations of constitutive models for cyclic interface response.

Keywords: constitutive models, contact interfaces, friction, dilatancy

1 Introduction

The problem of modelling of material interface response under monotonic and cyclic loading is of fundamental scientific and engineering importance. In fact, such interfaces occur in most engineering or geotechnical structures such as masonry structures, fibre-reinforced brittle matrix composites, jointed rock masses, dams, bridges, etc. The structural stiffness and limit load are strongly dependent on inelastic interface response. As the displacement discontinuity resulting from frictional slip along interface occurs, the localized effects of damage and wear develop depending on micro-mechanical effects of asperity interaction. A closely related problem of fluid transport along interfaces (essential, for instance, in nuclear waste storage technology), essentially coupled with the mechanical response, will not be discussed in the paper.

The present paper is devoted to the analysis of monotonic and cyclic effects at contact interfaces of brittle materials. The class of materials (and interfaces) is quite wide and includes: rock joints, artificial and natural joints in civil engineering structures, existing cracks in brittle materials (e.g. concrete, ceramics), masonry and other cementitious joints, fibre-matrix interfaces in brittle matrix composites, etc. A special attention is paid to interfacial dilatancy phenomena as this aspect does not seem to have been sufficiently

analyzed in the literature. Although the emphasis is laid on friction and dilatancy effects, some attention is also paid to tensile/compressive behaviour as these phenomena are coupled and cannot be completely separated.

Some of the interfaces considered in this work are characterized by initial tensile strength. Typical examples of cohesive interfaces are the masonry joints and fiber-matrix interfaces and also infilled rock joints. The decohesion process is understood as a loss of tensile strength along a predefined interface. Thus crack propagation problems in which the crack path is a part of the solution are not considered. This is the case of a weak interface between two dissimilar (or similar) materials. Clearly, the decohesion may occur in tension (mode I), shear (mode II/III) or mixed modes.

In the case of cohesive interfaces, the formation of the actual rough surface is a part of the deformation process. As a result the asperities of one surface match (at least partially) the asperities of the other surface. On the other hand, most of the non-cohesive interfaces studied in this paper (e.g. rock joints) are generated through the prior cracking processes. In such case the asperities of both contacting surfaces also match, depending on the mechanical and environmental conditions since the time of joint formation. The interaction of interlocked asperities strongly affects the friction and dilatancy response of these interfaces. This, in fact, is a common effect for most of the brittle interfaces.

In Section 2 the most important effects observed experimentally are presented followed by a qualitative discussion of the related micro-mechanical mechanisms. The constitutive models for brittle interfaces are discussed in Section 3. A critical review of existing interface models is provided and some new formulations of constitutive models of cyclic behaviour of interfaces are proposed.

2 Experimental effects of mechanical interface response

2.1 Typical experimental setups

Frictional properties of joints/interfaces are usually investigated by performing shear tests with uniform contact conditions along the interface, Fig. 1(a). In direct shear tests a constant normal pressure is kept during shearing, thus allowing for free dilation at the interface. Typically, the friction stress and the relative normal displacement (dilation) are measured as a function of relative tangential displacement (slip). These tests are typically performed for rock joints, masonry joints, etc., cf. for example Bandis et al. (1981), Atkinson et al. (1989).

The principle of tensile/compressive tests is similar to that of direct shearing, Fig. 1(b). The measured response is the normal pressure and relative normal displacement, cf. Bandis et al. (1983), van der Pluijm (1997).

The direct shear tests cannot be used for investigating the properties of fiber-matrix interfaces in brittle matrix composites because of very small dimensions of the fiber. Instead, single- or multiple-fiber pulling or pushing tests are usually applied, cf. Marshall et al. (1990,1992). In these tests, however, the contact conditions are not constant along the interface as the debonding zone and slip zone propagate along the interface with increasing load. Unlike in direct shear tests, the normal pressure at the interface cannot

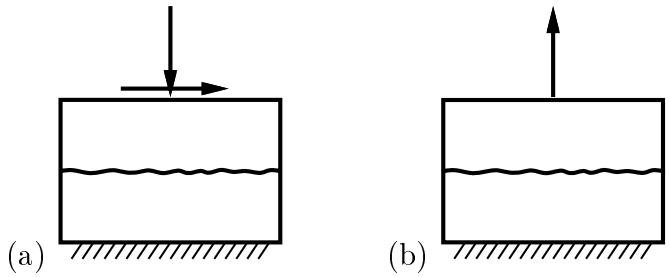

Figure 1: Scheme of uniform shearing (a) and tensile/compressive (b) tests on joints.

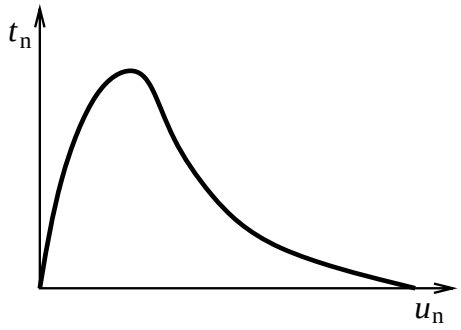

Figure 2: Typical tensile response of cohesive joints.

be varied, and also due to the matrix surrounding the fiber the interfacial dilation is constrained.

Clearly, other types of tests are performed depending on the joint/interface type and specific requirements. These, for example, include multiply-jointed rock specimens (Bandis et al., 1981), four point bending tests (van der Pluijm, 1997), shearing of masonry wall panels (Anthoine et al., 1995), etc., containing multiple interface systems.

2.2 Monotonic loading

2.2.1 Tension of cohesive joints

The tensile behaviour of cohesive interfaces resembles that of mode I fracture of the quasi-brittle materials (e.g. concrete), where after reaching a peak the strength decreases to zero, cf. Fig. 2 (we use a notation, in which the tensile contact stresses and opening relative displacements are positive). Masonry joints are typical examples of cohesive interfaces. Van der Pluijm (1997) investigated the response of masonry bed joints in tension. The fracture occurred at the interface between the mortar layer and one of the blocks (bricks). The results were characterized by a large scatter of results in terms of peak stresses, fracture energies and characteristic opening displacements for nominally identical specimens.

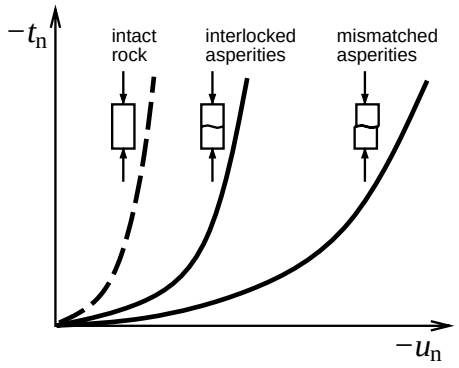

Figure 3: Typical compressive response of rock joints.

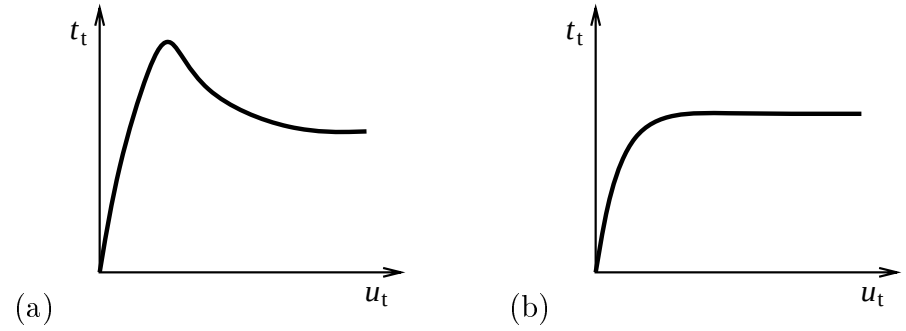

Figure 4: Typical response to direct shear tests: (a) with and (b) without peak.

2.2.2 Compression

Under compression the relation between the normal pressure and the normal relative displacement is nonlinear. Typical response curves for rock joints are given in Fig. 3, where two cases are shown namely a joint with interlocked (fully mated) asperities and with mismatched asperities, cf. Bandis et al. (1983), Sun et al. (1985). When the asperities are not interlocked the contact stiffness decreases as an effect of localized deformation at asperity contacts.

2.2.3 Shearing

The shearing response under constant normal pressure is usually characterized by a peak followed by softening until a residual shear stress is attained, Fig. 4(a). This type of behaviour is observed for both cohesive (Atkinson et al., 1989; van der Pluijm, 1993; Binda et al., 1994) and non-cohesive joints (Kutter et al., 1980). In the latter case, the response without the peak shear resistance may also be observed (Bandis et al., 1981; Sun et al., 1985), cf. Fig. 4(b). Generally, the post-peak softening can be attributed to several phenomena, often occurring simultaneously, namely to decohesion, configurational effects due to dilation, friction softening caused by damage and wear of asperities, etc. These topics are discussed in detail in Section 3 concerned with constitutive modelling of interfaces.

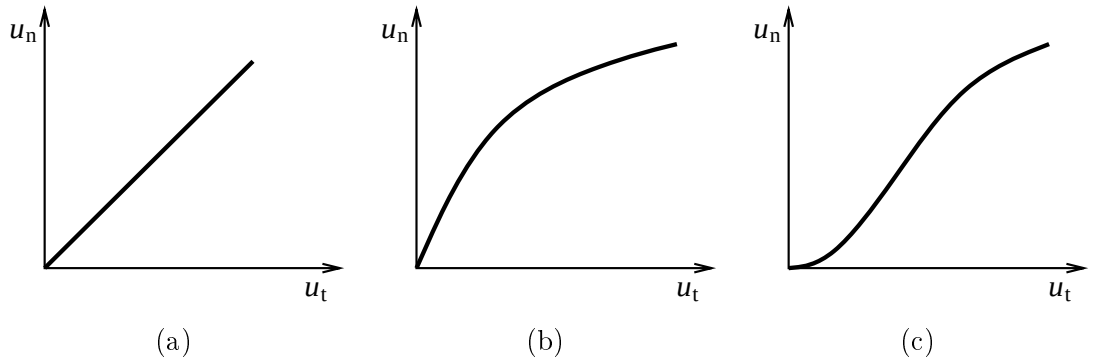

Figure 5: Typical dilation curves in monotonic direct shear tests.

The shearing displacement is usually accompanied by the dilation of the joint. Here several typical dilation curves are observed experimentally depending on the joint type, initial state of the joint and amount of shearing displacement applied in the test. Some joints show a nearly linear dilation response as indicated in Fig. 5(a). As the interfacial dilation has to be bounded, such response should be understood as an initial portion of a general nonlinear response with an asymptotic dilation occurring at sliding displacements high enough as compared to the characteristic length of primary asperities, Fig. 5(b). Finally, some joints are characterized by an increasing dilatancy angle at small shearing displacements, which then gradually decreases with increasing amount of sliding (provided the test is performed with large enough sliding displacements), Fig. 5(c).

An important effect is usually observed, namely that dilation is reduced with an increasing normal pressure. This effect is explained by asperity crushing at the values of normal pressures relatively high with respect to the unconfined compressive strength of the asperity material.

2.3 Non-monotonic and cyclic effects in shearing of joints

Generally, much less experimental results of cyclic tests are available as compared to monotonic tests. In this section, we only discuss the effects observed in cyclic shearing. The results of cyclic compression of rock joints can be found for example in Bandis et al. (1983) and Sun et al. (1985).

2.3.1 Reversible dilation component

As discussed previously, the joint opening (dilation) is commonly observed in the monotonic direct shear tests. However, upon unloading the dilation decreases until the shear displacement changes its sign and then increases again, Fig. 6(a,b). The actual shape of the cyclic dilatancy curve depends strongly on the joint type, normal stress and the range of applied shearing displacement. The reversible dilation effect is typical for natural (well-seated) rock joints (Kutter et al., 1980; Fox et al., 1998) and masonry joints (Atkinson et al., 1989). The phenomenon of reseating load drop in fiber push-back tests is also explained by the reversible dilation component at the fiber-matrix interface, cf.

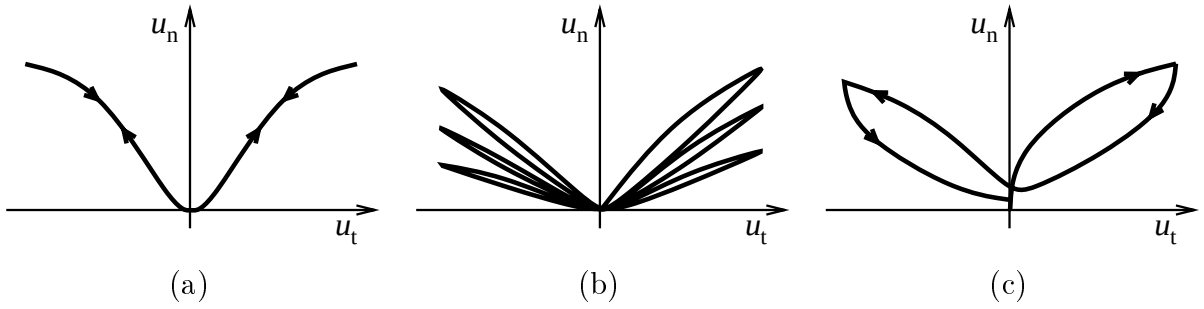

Figure 6: Cyclic dilatancy response: (a) rock joint under low normal pressure, (b) cyclic degradation of dilatancy, (c) masonry bed joint with a dilatancy drop at load reversal.

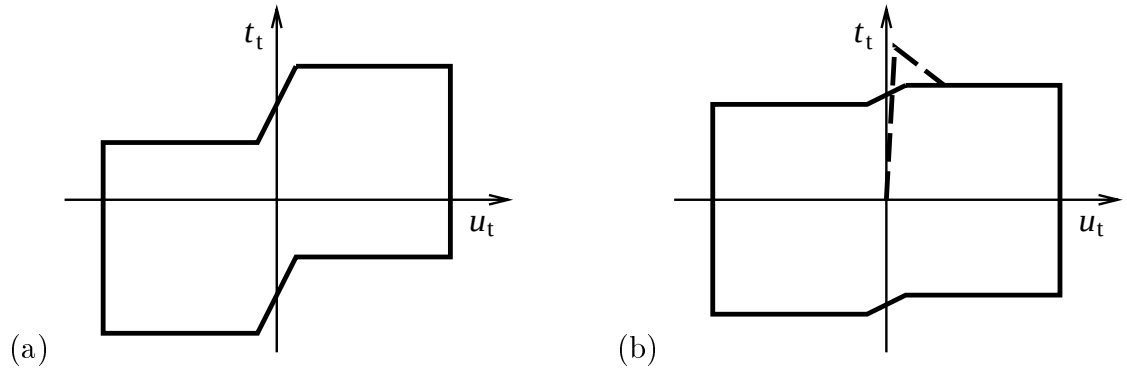

Figure 7: Idealized friction jump in the vicinity of original mated joint position: (a) strong, (b) weak effect.

Section 2.3.5.

2.3.2 Friction jump at zero relative displacement

This effect is commonly observed for many types of interfaces. In the case of initially mated rough rock joints the effect may be very strong with the friction stress increasing two-three times when the two contacting surfaces pass through their original position (i.e. at zero relative displacement), cf. Hutson and Dowding (1990), Fox et al. (1998). This case is sketched in Fig. 7(a). On the other hand, the effect is much weaker, but still visible, for other joints, as shown in Fig. 7(b), cf. results of Atkinson et al. (1989) for masonry bed joints. The dashed line in Fig. 7(b) represents the peak followed by softening during the first loading cycle observed both for cohesive joints (such as masonry joints) and some rock joints.

If the normal pressure is high enough to crush and wear the asperities, the jump decreases for consecutive loading cycles, cf. Kutter et al. (1980), Hutson and Dowding (1990), Jing (1990), Atkinson et al. (1989). Otherwise, the cyclic response is hardly affected by the number of loading cycles, cf. Hutson and Dowding (1990), Fox et al. (1998).

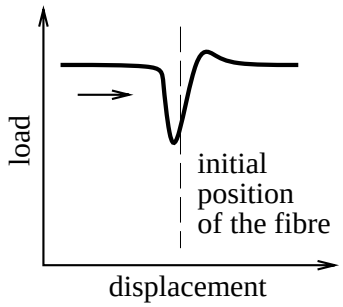

Figure 8: Reseating drop of the pushing load in a fibre push-back test.

2.3.3 Cyclic degradation of dilatancy

For repeated cyclic shearing the dilation decreases with increasing number of cycles. The higher the normal pressure with respect to the joint material strength the stronger the effect, cf. Hutson and Dowding (1990), Fox et al. (1998). A typical cyclic dilatancy curve of a rock joint under relatively high normal pressure is shown in Fig. 6(b), while for very low pressures the response resembles that in Fig. 6(a). Cyclic degradation of dilatancy is also observed in the case of masonry bed joints, cf. Atkinson et al. (1989).

2.3.4 Drop of dilation angle at load reversals

The results of cyclic shearing of masonry bed joints reported by Atkinson et al. (1989) are characterized by a significant drop of dilation angle at each load reversal, Fig. 6(c). This behaviour is qualitatively different from that of typical rock joints, cf. Fig. 6(a,b). As there is currently no theory explaining this behaviour it will be discussed in detail in the modelling part of the paper.

2.3.5 Reseating load drop in fiber push-back tests

Fiber pushing or pulling tests are commonly used to examine the properties of fiber-matrix interfaces in brittle matrix composites (BMC). The importance of interfacial dilation is well illustrated by, so called, push-back tests in which the fiber is first displaced from its original position (by pushing or pulling) and next pushed in the opposite direction. Once the fiber passes through its initial position the load required to push the fiber decreases and subsequently increases to the previous value, cf. 8. This phenomenon of *reseating drop* of the load has been observed by several authors, cf. Carter et al. (1991), Jero et al. (1991) and Cherouali et al. (1997). The explanation of the phenomenon is that the asperities of the fiber and matrix perfectly match in the original fiber position while after displacing the fiber, the interaction of asperities results in the dilation of the interface. As the dilation is constrained due to surrounding matrix, the normal pressure (and thus also the friction stress) increases when the fiber is moved from its initial position. Note that in these tests the displacement of the fiber is typically much larger than the characteristic asperity length, thus the dilation has a constant asymptotic value, except for a close vicinity of the original position.

Table 1: Summary of experimentally observed phenomena.

Monotonic loading	
A.1	quasi-brittle damage in tension, Fig. 2
A.2	decreased normal stiffness of mismatched joints, Fig. 3
A.3	peak resistance in direct shear, Fig. 4(a)
A.4	shearing response without peak stress, Fig. 4(b)
A.5	constant residual shearing resistance, Fig. 4(a) and 4(b)
A.6	dilation in direct shear, Fig. 5
A.7	decreasing dilation with increasing normal pressure
Cyclic loading	
B.1	reversible dilation component, Fig. 6(a)
B.2	friction jump at zero relative displacement, Fig.7
B.3	cyclic degradation of dilatancy, Fig. 6(b)
B.4	drop of dilation angle at load reversals, Fig. 6(c)
B.5	reseating load drop in fiber push-back

Table 2: Micro-mechanisms and related effects.

Mechanism	Related effects
decohesion	A.1, A.3, A.5, A.6
interaction of well-seated primary asperities	A.3, A.4, A.5, A.6, B.1, B.2, B.5
random asperity contact	A.2
wear/damage of primary asperities	A.7, B.3
wear/damage of secondary asperities	A.3, A.5
formation of a third body granular layer	B.4

2.4 Interpretation of observed phenomena

Before discussing constitutive models of interfacial behaviour we shall briefly provide a micro-mechanical explanation of the effects described above. The most important effects are summarized in Table 1. Each effect is assigned a number which will be referred to throughout the rest of the paper.

Now, we shall discuss the main micro-mechanical mechanisms that occur at brittle interfaces. In Table 2 we associate these mechanisms with the effects that are related to them. Note that some effects may be attributed to several mechanisms.

2.4.1 Decohesion

Decohesion is a fracture (damage) process which proceeds along a predefined, usually weaker interface. In terms of the mechanical response, the decohesion results in some peak strength followed by a softening regime, both in tension and in shear. When the

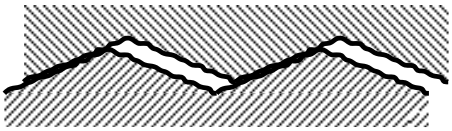

Figure 9: Primary and secondary asperities in an interlocked joint.

cohesive strength is lost, the tensile strength drops to zero (A.1), while in shear a residual frictional resistance is maintained (A.3, A.5). In the case of shearing (also under some compressive normal pressure), the decohesion process usually proceeds through a distributed damage process associated with volumetric deformation in the process zone, which leads to interfacial dilation (A.6).

2.4.2 Interaction of well-seated primary asperities

It is very well known that, regardless of the type of the contact pair, the surfaces in contact are rough and that asperity interaction is a fundamental mechanism governing contact phenomena. In the context of brittle interfaces two distinct cases may occur, namely

1. well-seated (interlocked) asperities,

2. random asperity contact.

Random asperity contact is a usual situation of contact of two non-correlated surfaces. On the contrary, the case of well-seated asperities is typical for brittle interfaces where the contact surface with its roughness (asperities) is a result of a crack propagation process (decohesion of a cohesive interface or a crack that formed the joint in the past).

The surface roughness may be seen as a composition of asperities of different length scales. A simplifying assumption is often adopted, namely two scales of asperities are considered: primary asperities (the largest ones) and secondary asperities, cf. Mróz and Giambanco (1996), Mróz and Stupkiewicz (1994,1998). This assumption allows to separate the basic mechanisms in a clear way, although in reality the interactions of asperities of different scales are coupled. In this work we assume that the primary asperities are responsible for interfacial dilation, while the secondary asperities govern the friction conditions at the inclined contacts of primary asperities, cf. Fig. 9.

The interaction of well-seated primary asperities is a basic mechanism explaining the dilation effects in joints. Depending on the shape of asperities different dilatancy curves in direct shear (A.6) may be generated, cf. Fig. 5. Also the shear resistance response with peak (A.3) or without peak (A.4), as well as a constant residual resistance (A.5), may be predicted depending on the asperity shape and the range of relative displacements considered. Finally, in cyclic shearing the change from downward to upward sliding results in an increase of friction (B.2). These topics are discussed in detail in Section 3.2.

2.4.3 Random asperity contact

It is natural to expect that randomly contacting asperities are less stiff and easier to be crushed than the well-seated asperities (A.2). In shearing, there are no dilation effects

observed for well-seated asperities, however, the wear and damage of asperities may result in compaction at the interface. Let us note, that the random contact of asperities occurs after a joint with interlocked asperities undergoes a shearing displacement larger than the characteristic length of primary asperities (assuming the asperities are not ideally periodic).

2.4.4 Wear and damage of primary asperities

Wear and damage of initially interlocked primary asperities result in a decrease of dilation for subsequent cycles (B.3). Also the high contact pressures accelerate the wear/damage process and lead to a further decrease of the effective dilation angle (A.7).

2.4.5 Wear and damage of secondary asperities

The frictional properties at the inclined contacts of primary asperities are governed by the secondary asperities. These also undergo damage and wear in the course of relative sliding, thus the effective friction properties evolve. In particular, a peak followed by a residual friction stress may be associated with wear and damage of secondary asperities (A.3, A.5).

2.4.6 Formation of a third body granular layer

The surface damage associated with asperity crushing and wear leads to the formation of a third body layer. This layer consists of free particles of different sizes and may be seen as a granular material. While this fact seems to be well recognized, the respective models are not available. In Section 3.3 we propose a phenomenological model of a granular third body layer. In particular, the effect of the drop of dilation angle at the load reversals (B.4) may be attributed to the rearrangement of free particles due to the change of shearing direction.

3 Constitutive interface models

In this section we review the existing models with respect to their ability to describe the basic effects discussed in the previous section. A new constitutive interface model will also be discussed in Section 3.3. The analysis of this section is mostly qualitative as we concentrate on the effects rather than on reproducing experimental data exactly. For simplicity, we restrict our analysis to two-dimensional problems. Extension to general three-dimensional problems will be presented elsewhere.

A general model of friction is formulated using a friction condition $F \leq 0$ and a slip potential $G = \text{const}$. The actual forms of functions F and G depend on the specific model types and will be stated for each considered model.

In the plasticity theory approach to friction, the total relative velocity $\dot{\boldsymbol{u}} = \{\dot{u}_t, \dot{u}_n\}^T$ is decomposed into elastic $\dot{\boldsymbol{u}}^e$ and inelastic $\dot{\boldsymbol{u}}^s$ components

$$\dot{\boldsymbol{u}} = \dot{\boldsymbol{u}}^e + \dot{\boldsymbol{u}}^s \tag{3.1}$$

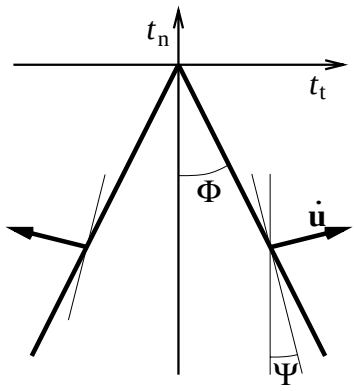

Figure 10: Limit friction surface of the Coulomb law.

and the rate of contact traction $\dot{\boldsymbol{t}} = \{\dot{t}_t, \dot{t}_n\}^T$ is related to the elastic velocity components by the rule

$$\dot{\boldsymbol{t}} = \boldsymbol{D}\dot{\boldsymbol{u}}^e, \quad \boldsymbol{D} = \begin{bmatrix} k_t & 0 \\ 0 & k_n \end{bmatrix} \tag{3.2}$$

where k_n, k_t are the normal and tangential contact stiffness parameters, which may generally depend on contact stresses and the respective state variables. The slip potential $G = \text{const}$ generates the following slip rule

$$\dot{\boldsymbol{u}}^s = \dot{\lambda}\frac{\partial G}{\partial \boldsymbol{t}}, \quad \dot{\lambda} \geq 0, \quad \dot{\lambda}F = 0 \tag{3.3}$$

where $\dot{\lambda}$ is a plastic multiplier.

3.1 Coulomb-type laws

Let us first introduce a simple prototype law as a basis for further discussion of prediction capabilities and possible enhancements. The limit friction surface $F = 0$ of the Coulomb law is a cone in the space of contact tractions, cf. Fig. 10, described by the friction condition

$$F(t_n, t_t) = |t_t| + t_n \tan\Phi \leq 0 \tag{3.4}$$

accompanied by the slip potential

$$G(t_n, t_t) = |t_t| + t_n \tan\Psi \tag{3.5}$$

Here, Φ and Ψ denote the friction and dilatancy angles, which are the constitutive parameters of the model. The slip rule now takes the form

$$\dot{\boldsymbol{u}}^s = \dot{\lambda}\frac{\partial G}{\partial \boldsymbol{t}} = \dot{\lambda}\boldsymbol{m}, \quad \boldsymbol{m} = \{s, \tan\Psi\}^T, \quad s = \frac{t_t}{|t_t|} \tag{3.6}$$

where $s = \pm 1$ is the direction of slip.

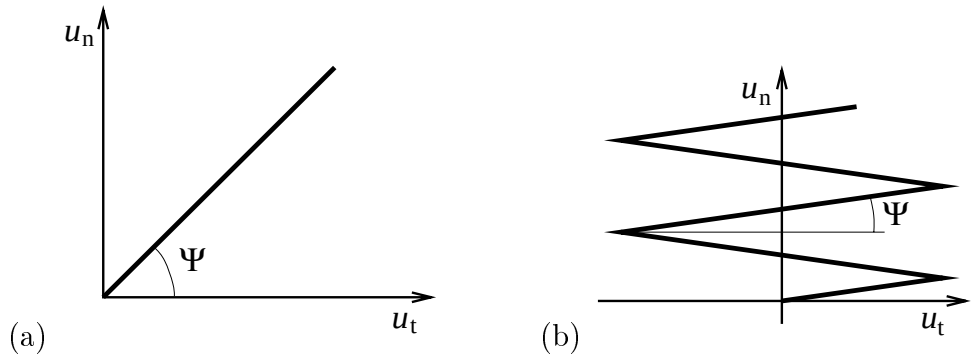

Figure 11: Dilatancy response of a simple Coulomb law: (a) monotonic and (b) cyclic shearing.

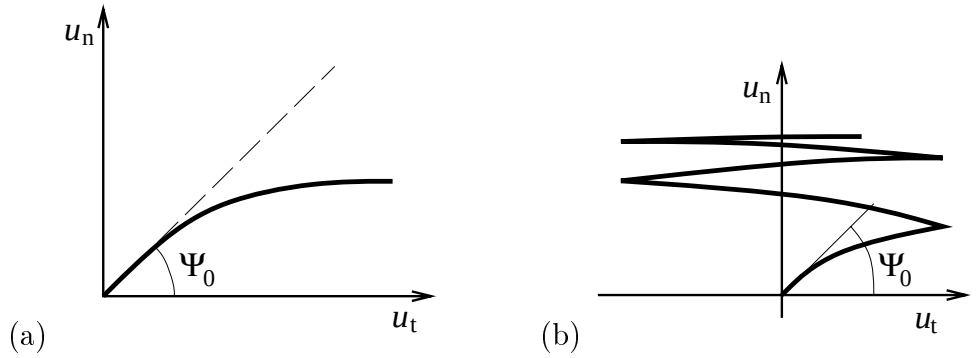

Figure 12: Dilatancy response of a Coulomb law with decreasing dilation angle: (a) monotonic and (b) cyclic shearing.

Equation (3.6) predicts sliding inclined at a constant dilatancy angle Ψ with respect to the nominal contact plane. The monotonic and cyclic dilatancy curves are schematically plotted in Fig. 11. Clearly, the predicted response is highly idealized. Firstly, the dilation is not limited as the shear displacement increases. Secondly, the cyclic response is completely different from that observed experimentally, cf. Fig. 6. Thus the applicability of this law is limited to monotonic processes and small shear displacements.

An excessive dilation predicted by the Coulomb law at large shear displacements may be avoided by assuming an evolution rule for the dilation angle, for example in the following simple form

$$\Psi = \Psi_0 e^{-\kappa_\Psi/\bar{\kappa}_\Psi} \tag{3.7}$$

where Ψ_0 is an initial dilation angle, κ_Ψ is a state variable governing the evolution of dilation angle and $\bar{\kappa}_\Psi$ is a material parameter governing the rate of variation of the dilation angle. By analogy to work (or strain) hardening variables in the plasticity theory, the evolution variable κ_Ψ may be defined as follows

$$\dot{\kappa}_\Psi = t_t \dot{u}_t^s \quad \text{or} \quad \dot{\kappa}_\Psi = |\dot{u}_t^s| \tag{3.8}$$

The dilation in monotonic shearing is now limited, cf. Fig. 12(a), and thus more realistic.

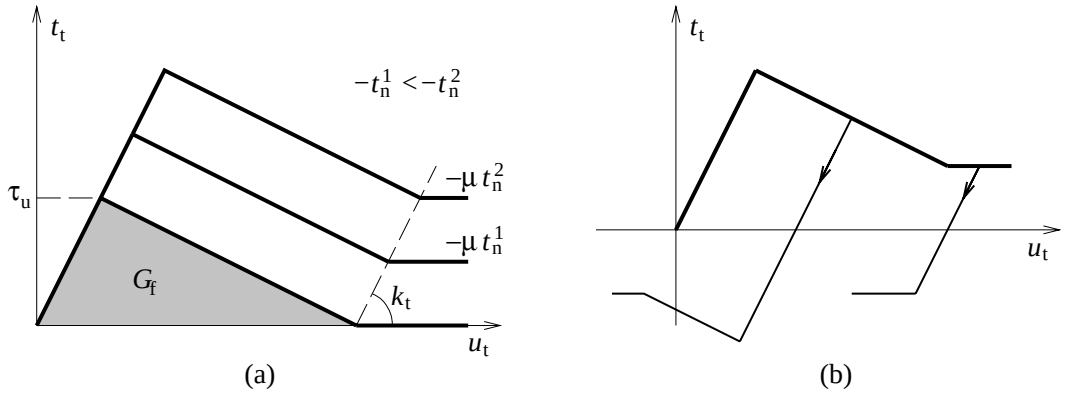

Figure 13: The response of the cohesive Coulomb law in direct shear: (a) monotonic loading; (b) unloading response.

However, the cyclic response is still qualitatively different from that observed experimentally, Fig. 12(b).

The simple Coulomb law can be modified to include the effects of decohesion and softening response of the interface. Assume the yield surface is the form

$$F(t_n, t_t, \eta) = |t_t| + \mu t_n - (1-\eta)\tau_u \leq 0 \tag{3.9}$$

where $0 \leq \eta \leq 1$ is a damage-like variable. The evolution of η is governed by

$$\dot{\eta} = \frac{|\dot{u}_t^s|}{u_t^{\rm cr}}, \quad \text{for } \eta < 1 \tag{3.10}$$

where $u_t^{\rm cr} = 2G_f/\tau_u$. When $\eta = 1$ a loss of cohesion occurs and a pure Coulomb friction model is obtained. The parameters of the model are the ultimate shear strength τ_u, specific fracture energy G_f and residual friction coefficient μ. The response of the model is depicted in Fig. 13. As the model is very simple, it does not properly describe tensile and mixed tensile-shear decohesion modes.

Several interface models have been derived from the Coulomb law by adding cohesion with hardening/softening effects and evolution rules for dilation angle, cf. Gens et al. (1989), Lotfi and Shing (1994), Gambarotta and Lagomarsino (1997), Lourenco and Rots (1997), Raous et al. (1999). The simple Coulomb's cone has been replaced by a hyperbolic limit surface (with a hyperbolic sliding potential) to better model mixed mode decohesion and the effect of normal stress on friction and dilation by Lotfi and Shing (1994). A model with additional surfaces related to tensile and compressive damage has been proposed by Lourenco and Rots (1997).

In these Coulomb-type interface laws much effort has been put to capture several important effects of the friction (peak and residual resistance, decohesion) and dilation response in monotonic loading processes. As a result, the monotonic behaviour of different types of joints is well described by these models. However, the cyclic effects, cf. Tables 1 and 2, which origin from the interaction of interlocked asperities are completely ignored in these models. Particularly, the cyclic dilation behaviour, Fig. 12(b), is unacceptable as compared to the actual typical response, cf. Fig. 6.

Figure 14: Configurational dilation resulting from interaction of initially matching primary asperities: (a) $u_t^s = 0$, $u_n^s = 0$; (b) $0 < |u_t^s| < u_A$, $0 < u_n^s < \delta_A$; (c) $|u_t^s| > u_A$, $u_n^s > \delta_A$.

3.2 Asperity interaction models

3.2.1 Configurational dilatancy model

Let us first introduce a simple model of fully reversible configurational dilation. The dilation is assumed to solely result from the interaction of interlocked asperities. The wear and damage of asperities as well as initial cohesion of the joint are neglected at this stage, thus no irreversible dilatancy effects occur.

The interaction of initially well-seated asperities is schematically illustrated in Fig. 14. Since wear and damage of asperities are neglected we can assume that dilation depends only on the shearing displacement of the joint, cf. the concept of the *relative displacement surface of sliding* introduced by Gerrard (1986). A physically acceptable and consistent model requires that the dilation is limited with increasing shearing displacement. The following function is adopted to describe the dilation function $\delta(u_t^s)$, cf. Stupkiewicz (1996),

$$u_n^s = \delta(u_t^s) = \delta_A \delta_u(u_t^s/u_A) \tag{3.11}$$

where δ_A and u_A denote the characteristic height and length of primary asperities. The dimensionless function δ_u defines the actual shape of the dilation response curve and must satisfy two conditions, namely $\delta_u(0) = 0$ (i.e. no dilation in the absence of shearing displacement) and $\delta_u(\pm\infty) = 1$ (i.e. asymptotic dilation equal to δ_A).

Some insight into possible forms of the function δ_u can be gained by studying the interaction of periodic asperities. Periodic saw-tooth and sine-shaped asperities are shown together with respective dilation curves in Fig. 15. Note that the periodicity assumption leads to a non-physical dilation decrease once the asperity peaks enter neighbouring valleys, cf. dashed lines in Fig. 15. As the real asperities are not periodic it is reasonable to assume that after the asperities leave their initial valleys, the random contact of asperity peaks occurs resulting in a constant dilation for $u_t^s > u_A$.

The local asperity contacts are inclined with respect to the nominal contact plane. We shall assume that friction at the inclined contacts of primary asperities is governed by the Coulomb law (with no dilation). Thus the effective friction angle for sliding in an upward direction is $\Phi + |\Psi_c|$ and in a downward direction is $\Phi - |\Psi_c|$, cf. Fig. 16. The angle of configurational dilatancy Ψ_c follows from (3.11)

$$\Psi_c = \frac{\mathrm{d}\delta}{\mathrm{d}u_t^s} \tag{3.12}$$

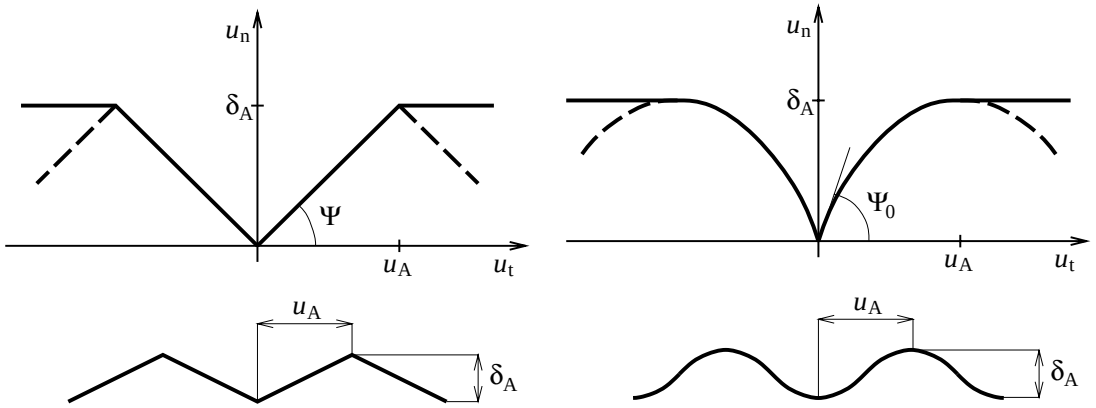

(a) (b)

Figure 15: Dilation curves resulting from the assumption of periodic saw-tooth (a) and sine-shaped (b) asperities.

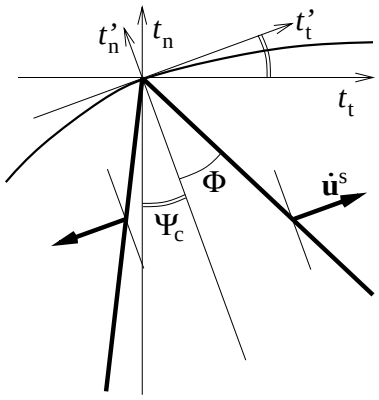

Figure 16: Friction condition at an inclined contact of primary asperities.

The limit friction condition can be formulated using global contact stresses t_t, t_n or in a rotated coordinate system using local stresses t'_t, t'_n, cf. Fig. 16. In the space of global stresses the limit friction condition and the sliding potential have the form

$$\begin{array}{rcl} F(t_n, t_t) & = & st_t + t_n \tan(\Phi + s\Psi_c) \leq 0 \\ G(t_n, t_t) & = & st_t + t_n \tan(\Psi + s\Psi_c) \end{array} \tag{3.13}$$

where Ψ is the dilation angle at the inclined contact of primary asperities [for $\Psi = 0$ only the dilatancy resulting from the interaction of primary asperities is modeled, cf. (3.11)]. Note that here the sliding direction factor $s = \pm 1$ is explicitly involved in the description. In the case of $\Phi < |\Psi_c|$ the direction of sliding is different from the direction of friction stress thus $s = \text{sign}\dot{u}_t$ should be used in eqn. (3.13) rather than $s = \text{sign}t_t$ as in eqn. (3.6).

Alternatively, the limit condition can be formulated in terms of local stresses t'_t, t'_n, namely

$$\begin{array}{rcl} F'(t'_n, t'_t) & = & |t'_t| + t'_n \tan\Phi \leq 0 \\ G'(t'_n, t'_t) & = & |t'_t| + t'_n \tan\Psi \end{array} \tag{3.14}$$

While the limit friction condition and sliding potential are exactly the same as in case of the Coulomb law (3.4)–(3.5), the coordinate system rotates as the dilation angle changes

$$\boldsymbol{t}' = \boldsymbol{Q}\boldsymbol{t}, \quad \dot{\boldsymbol{u}}' = \boldsymbol{Q}\dot{\boldsymbol{u}} \tag{3.15}$$

where

$$\boldsymbol{Q} = \begin{bmatrix} \cos\Psi_c & \sin\Psi_c \\ -\sin\Psi_c & \cos\Psi_c \end{bmatrix}, \quad \boldsymbol{Q}^T = \boldsymbol{Q}^{-1} \tag{3.16}$$

Although the description is simpler, the respective incremental relations involve the rotation velocity terms since $\dot{\Psi}_c \neq 0$.

The slip rule takes now the form

$$\dot{\boldsymbol{u}}'^s = \dot{\lambda}' \frac{\partial G'}{\partial \boldsymbol{t}'} = \dot{\lambda}' \boldsymbol{m}', \quad \boldsymbol{m}' = \{s', \tan\Psi\}^T, \quad s' = \frac{t'_t}{|t'_t|} \tag{3.17}$$

The slip direction in the global coordinate system is obtained by rotating $\dot{\boldsymbol{u}}'^s$, thus

$$\dot{\boldsymbol{u}}^s = \boldsymbol{Q}^T \dot{\boldsymbol{u}}'^s = \dot{\lambda}' \boldsymbol{Q}^T \boldsymbol{m}' = \dot{\lambda}' \boldsymbol{m} \tag{3.18}$$

and the resulting effective dilatancy angle is $\dot{u}^s_n / \dot{u}^s_t = \tan(\Psi_c + s'\Psi)$, in agreement with (3.13).

By putting $\Psi = 0$ a model with reversible configurational dilatancy is obtained. The model is fully defined by the friction angle Φ and the dilatancy curve $\delta(u^s_t)$. Some typical dilatancy curves and resulting friction response curves in cyclic direct shear are sketched in Fig. 17. The curves in Fig. 17(a,b) predict an unlimited dilation with increasing shear displacement and are thus only suitable for small relative displacements. Note, however, that similar response may be obtained by assuming the dilation curves of Fig. 17(c,d) with a small shear displacement amplitude. The curves in Fig. 17(a,c) have a singular point at $u^s_t = 0$. While this is close to the behaviour observed experimentally it would lead to numerical problems when applying the model in structural analysis. Assuming a

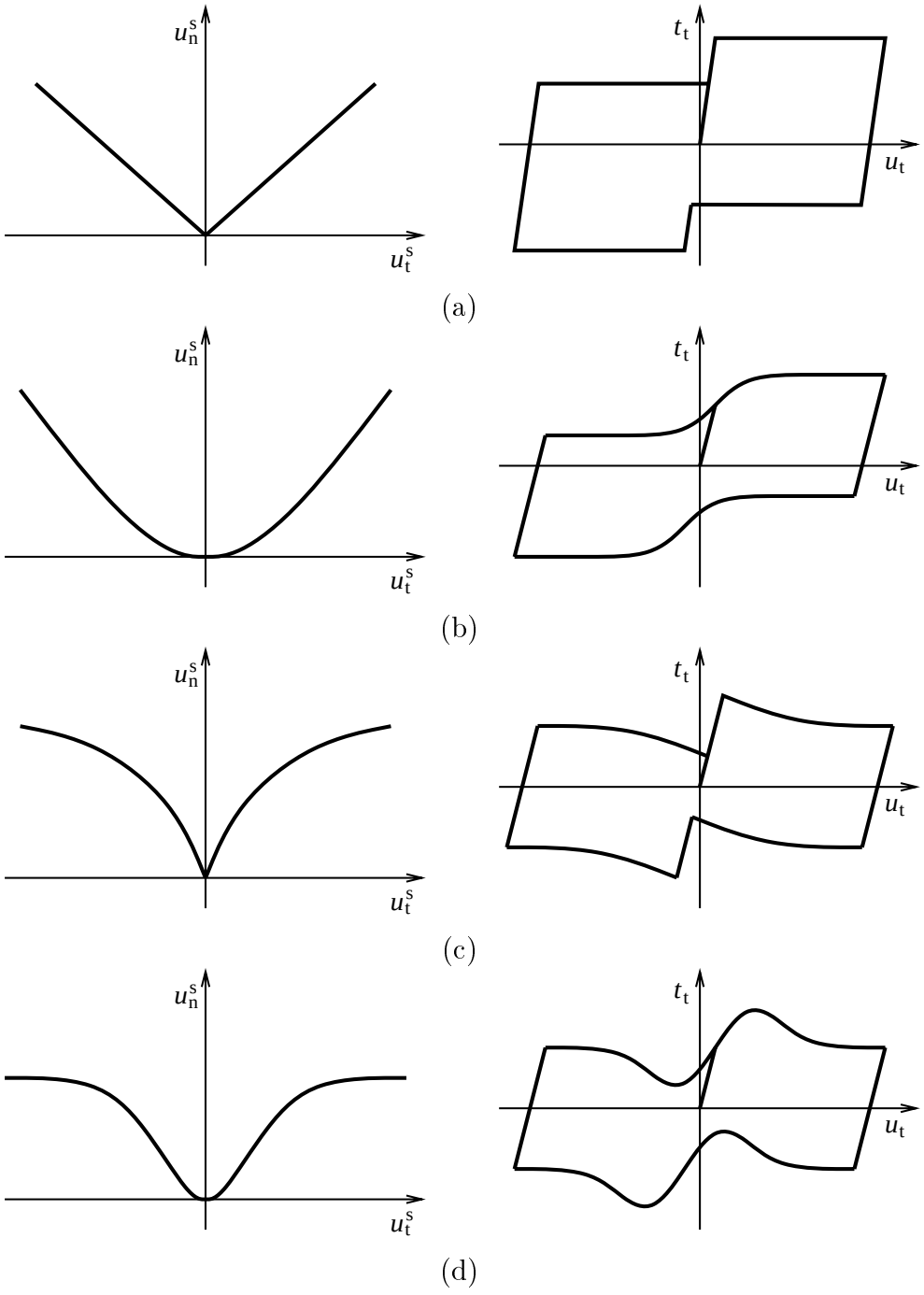

Figure 17: Configurational dilation: typical dilation curves and resulting cyclic shear response.

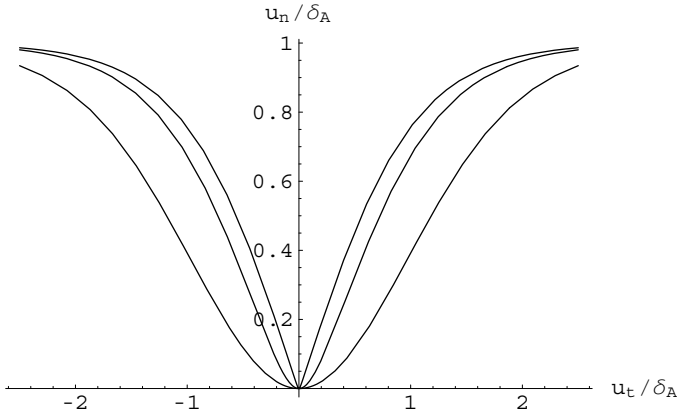

Figure 18: The effect of g_0 on the dilation curve (3.19) for $g_0/\delta_A = 0.01, 0.2, 1.$.

dilatancy curve with a non-zero radius at $u_t^s = 0$ is also justified in view of asperity wear and damage during relative sliding.

The specific form of the configurational dilation curve used in the current study is given by

$$u_n^s = \delta(u_t^s) = \delta_A \tanh\left[\frac{[(u_t^s \tan\Psi_0)^2 + g_0^2]^{1/2} - g_0}{\delta_A}\right] \tag{3.19}$$

where δ_A is the asperity height, g_0 is a parameter defining the radius of the dilation curve at $u_t^s = 0$ and Ψ_0 is the initial dilation angle in case of $g_0 = 0$. For small values of g_0 a nearly singular curve is obtained, while with increasing g_0 the radius also increases, cf. Fig. 18. Let us note that by choosing proper values of model parameters all the typical dilation curves depicted in Fig. 17 may be described by eqn. (3.19).

3.2.2 Asperity wear and damage

The effect of asperity wear and damage can be accounted for by assuming the dilation curve to additionally depend on the friction work. A simple model of this form has been proposed by Stupkiewicz (1996), by assuming the asperity height δ_A, cf. eqn. (3.11) and (3.19), to decreases due to the accumulated friction work.

Let us consider the slip rule resulting from the model of configurational dilation with wear and damage effects. We assume an explicit relation between the dilation u_n^s, relative sliding distance u_t^s and the accumulated friction work κ_δ, where

$$\dot\kappa_\delta = t_t \dot u_t^s \tag{3.20}$$

Note that other variables governing the wear effects may also be used, e.g. $\dot\kappa_\delta = t_t\dot u_t^s + t_n \dot u_n^s$ or $\dot\kappa_\delta = t_t' \dot u_t'^s$. By taking the time derivative of the relation $u_n^s = \delta(u_t^s, \kappa_\delta)$ we have

$$\dot u_n^s = \frac{\partial\delta}{\partial u_t^s}\dot u_t^s + \frac{\partial\delta}{\partial\kappa_\delta}\dot\kappa_\delta = \tan\Psi_c \dot u_t^s + \frac{\partial\delta}{\partial\kappa_\delta} t_t \dot u_t^s = \left[\tan\Psi_c - s\frac{\partial\delta}{\partial\kappa_\delta} t_n \tan(\Phi + s\Psi_c)\right]\dot u_t^s \tag{3.21}$$

where the limit friction condition $(3.13)_1$ has also been used. Thus in addition to the configurational dilation there is a compaction term resulting from wear. With increasing

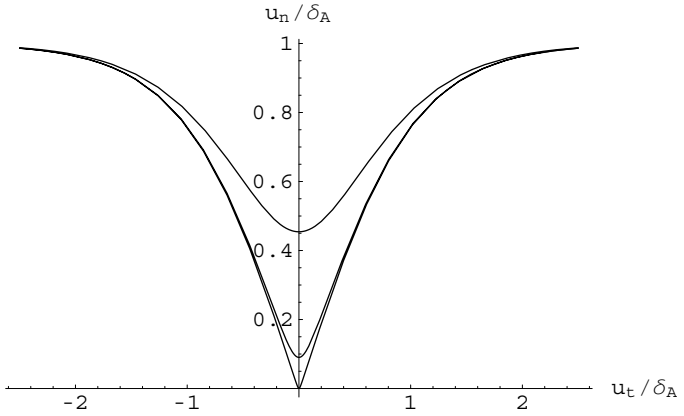

Figure 19: The effect of g on the dilation curve (3.22) with $g_0/\delta_A = 0.01$ and for $g/\delta_A = 0, 0.1, 0.5$.

normal pressure this additional term increases and the dilation is reduced, cf. effect A.7 in Table 1.

Adopting the dilation curve (3.19) the wear effect can be accounted for by assuming that the asperity height decreases due to accumulated friction work κ_δ, thus

$$u_n^s = \delta(u_t^s, \kappa_\delta) = \delta_A e^{-\kappa_\delta/\bar{\kappa}_\delta} \tanh\left[\frac{[(u_t^s \tan\Psi_0)^2 + g^2 + g_0^2]^{1/2} - g_0}{\delta_A}\right] \tag{3.22}$$

We also assume that the deposition of wear debris results in a decrease of curvature of the dilation curve at $u_t^s = 0$. The latter effect is governed by the term $g = g_f(1 - e^{-\kappa_\delta/\bar{\kappa}_g})$ in eqn. (3.22). The effect of increasing g on the dilation curve (3.22) is illustrated in Fig. 19. The parameters of the model related to wear effects are $\bar{\kappa}_\delta$, $\bar{\kappa}_g$ and g_f.

Two examples of cyclic response with wear effects are shown in Fig. 20. The response in Fig. 20(a) is obtained with $1/\bar{\kappa}_g = 0$ so that the wear effects are only due to decreasing asperity height.

Friction and dilation models based on the interaction of interlocked asperities have been studied by several authors and start from the works of Patton (1966) and Jaeger (1971) who considered wedge-like asperities and a constant dilation angle. Models with dilation angle decreasing with increasing shear displacement have been proposed by Plesha (1987), Snyman and Martin (1992) and Mróz and Giambanco (1996). Additional effects, such as the effect of wear on asperity slope (and dilation angle), as well as independent evolution of "right" and "left" asperity slopes, have also been accounted for by Plesha (1987). Mróz and Giambanco (1996) additionally considered the micro-slip phenomena, and Giambanco and Di Gati (1997) extended the asperity interaction mode by adding cohesion and softening effects.

As the wear effects are considered, the main difference between the current approach (cf. Stupkiewicz, 1996) and the works mentioned above is that we postulate dilation as an explicit function of relative displacement, friction work and possibly other state variables. In other models (Plesha, 1987; Mróz and Giambanco, 1996) it is the dilation angle that is specified as a function of relative displacement and friction work. In our approach the

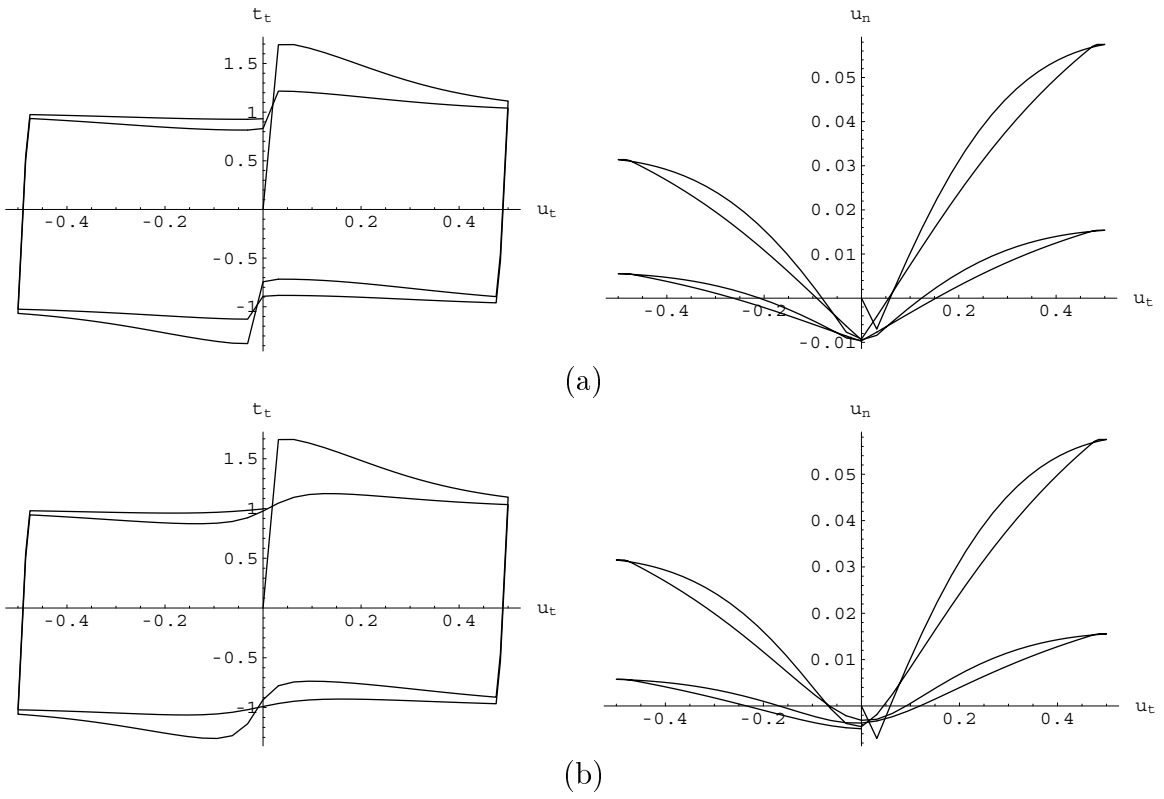

Figure 20: Configurational dilation with wear effects: friction and dilation response for (a) $1/\bar{\kappa}_g = 0$ and (b) $1/\bar{\kappa}_g > 0$.

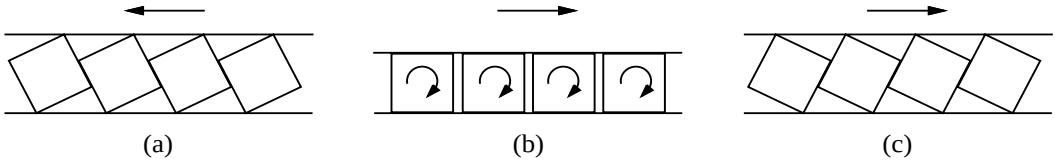

Figure 21: Configuration rearrangement of particles after the change of sliding direction.

current dilation angle follows from eqn. (3.21) and is different from the configurational dilation angle Ψ_c which defines the rotated contact tractions t'_t and t'_n.

3.3 Phenomenological model of a third body granular layer

In this section we propose a phenomenological description of a third body granular layer. Asperity wear and damage and, more generally, also surface wear at the contact interface lead to formation of a third body layer consisting of wear debris and particles of crushed material of contacting bodies. In the case of brittle materials this layer can be assumed to be a layer of granular material with particles of different sizes. While the fact of formation of such third body layer seems to be well-recognized, there are no models describing its effects on the interface response. Further, as already mentioned in Section 2.4, the effect of dilation angle drop [cf. Section 2.3.4 and Fig. 6(c)] cannot be explained by any of the known micro-mechanical interaction modes. We propose an explanation of this effect by considering the rearrangement of free third body particles at the interface.

Consider two bodies in contact separated by a layer of granular material. Upon shearing in one direction a steady state configuration of particles occurs. This is schematically illustrated in Fig. 21(a). If now a change of sliding direction takes place, the configuration of particles is rearranged, Fig. 21(b), and after some shear displacement related to the transient a steady state configuration associated with sliding in an opposite direction is obtained, Fig. 21(c). As schematically illustrated in Fig. 21 the change of sliding direction results in compaction and subsequent dilation of the interface during a transient particle rearrangement process.

In order to describe the memory associated with configuration of particles in the layer we shall introduce a rotating yield surface $F = 0$ moving within the steady state surface $F_s = 0$ as illustrated in Fig. 22. The steady state surface $F_s = 0$ is characterized by a friction angle Φ_s (dashed lines in Fig. 22)

$$F_s(t_n, t_t) = |t_t| + t_n \tan \Phi_s = 0 \tag{3.23}$$

and dilation angle Ψ_s so that the steady state slip potential is

$$G_s(t_n, t_t) = |t_t| + t_n \tan \Psi_s \tag{3.24}$$

The actual yield surface $F = 0$ is presented in a coordinate system rotated by angle Θ with respect to the nominal contact plane

$$F(t'_n, t'_t) = |t'_t| + t'_n \tan \Phi = 0 \tag{3.25}$$

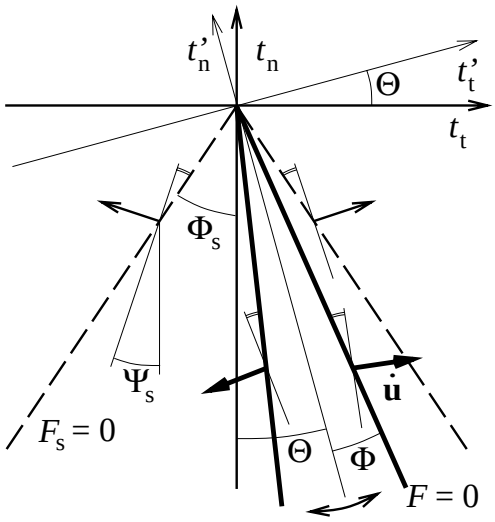

Figure 22: Rotating yield surface model for granular layer.

where $\Phi < \Phi_s$ and

$$\boldsymbol{t}' = \boldsymbol{Q}\boldsymbol{t}, \quad \boldsymbol{Q} = \begin{bmatrix} \cos\Theta & \sin\Theta \\ -\sin\Theta & \cos\Theta \end{bmatrix} \tag{3.26}$$

The concept of a rotating cone adopted in the present model is similar to the kinematic hardening model for sand proposed by Gajo and Muir Wood (1999). The slip rule is generated by the slip potential

$$G(t'_n, t'_t) = |t'_t| + t'_n \tan\Psi \tag{3.27}$$

so that

$$\dot{\boldsymbol{u}}'^s = \dot{\lambda}' \frac{\partial G'}{\partial \boldsymbol{t}'} = \dot{\lambda}' \boldsymbol{m}', \quad \boldsymbol{m}' = \{s', \tan\Psi\}^T, \quad s' = \frac{t'_t}{|t'_t|} \tag{3.28}$$

where $\dot{\boldsymbol{u}}'^s = \boldsymbol{Q}\dot{\boldsymbol{u}}^s$ is the (inelastic) relative velocity in the rotated coordinate system. Note that the effective dilation angle (i.e. the dilation angle in the global coordinate system) is

$$\Psi_{\text{eff}} = \arctan \frac{\dot{u}^s_n}{|\dot{u}^s_t|} = s'\Theta + \Psi \tag{3.29}$$

where $\Psi_{\text{eff}} > 0$ for $\dot{u}^s_n > 0$ (dilation) and $\Psi_{\text{eff}} < 0$ for $\dot{u}^s_n < 0$ (compaction).

In the steady state the stress point lies on the steady state surface $F_s = 0$ so that the rotation angle Θ equals to $\Theta_s = s'(\Phi_s - \Phi)$. Thus we assume a simple law to describe the evolution of Θ in the transient state

$$\dot{\Theta} = [s'(\Phi_s - \Phi) - \Theta] \frac{\dot{\kappa}_\Theta}{\bar{\kappa}_\Theta} \tag{3.30}$$

where the hardening variable κ_Θ is defined by (other forms including frictional work are also possible)

$$\dot{\kappa}_\Theta = |\dot{u}^s_t| \tag{3.31}$$

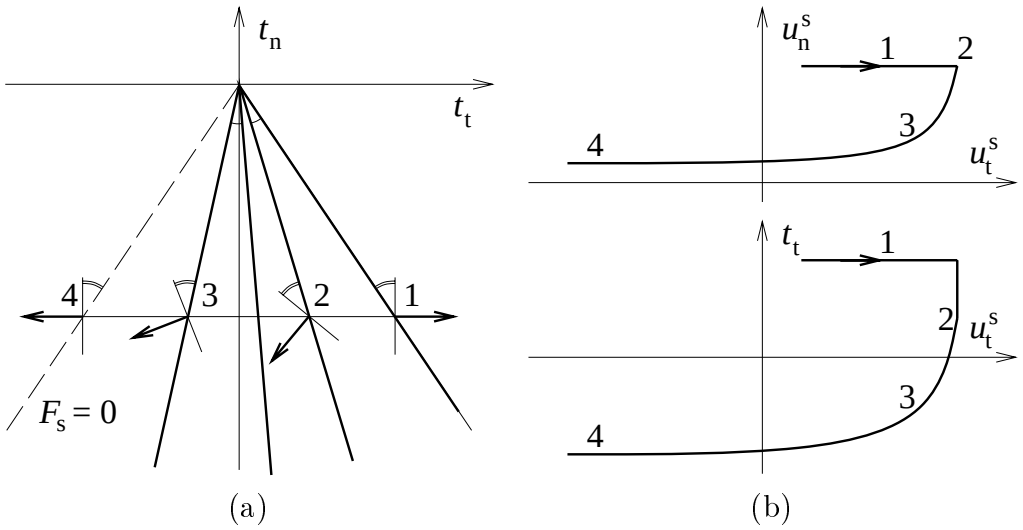

Figure 23: Rotating cone model (with $\Psi_s = 0$): (a) evolution of the yield surface upon load reversal; (b) dilatancy and frictional response.

and $\bar{\kappa}_\Theta$ is a model parameter (i.e. a characteristic sliding displacement related to the rotation of the yield surface $F = 0$).

We also assume that in the steady state the effective dilation angle Ψ_{eff} is equal to the steady state dilation angle Ψ_s. This condition provides the following relation between the dilation angles Ψ and Ψ_s

$$\Psi = \Psi_s - s'\Theta_s = \Psi_s - (\Phi_s - \Phi) \tag{3.32}$$

which, importantly, is assumed to hold also in the transient states.

As the dilation behaviour is the most important part of this model, let us illustrate the assumptions (3.30) and (3.32) in the case of shearing at constant normal pressure. Assume that the steady state dilation angle is constant and equal to $\Psi_s = 0$ and consider a steady state sliding situation with $\dot{u}_t^s > 0$. Since $\Psi_s = 0$ the normal relative velocity is $\dot{u}_n^s = 0$, cf. point 1 in Fig. 23. When the friction stress is reduced sliding in an opposite direction occurs after some elastic unloading stage—point 2 in Fig. 23. Note that the effective dilation angle at point 2 is $\Psi_{\text{eff}} = -2\Theta = -2(\Phi_s - \Phi)$ thus sliding in an opposite direction is associated with non-zero compaction velocity, Fig. 23(b). We can integrate (3.30) along the path 2–3–4 analytically, so that

$$\Theta = (\Phi_s - \Phi)[2e^{(u_t^s - \tilde{u}_t^s)/\bar{\kappa}_\Theta} - 1] \tag{3.33}$$

where $\tilde{u}_t^s \leq 0$ is the sliding displacement at load reversal.

Assuming that the effective dilation angle Ψ_{eff} is small we can write for $s' = -1$

$$\mathrm{d}u_n^s = \Psi_{\text{eff}}|\mathrm{d}u_t^s| = (s'\Theta + \Psi)s'\mathrm{d}u_t^s = (\Theta - \Psi)\mathrm{d}u_t^s = 2(\Phi_s - \Phi)e^{(u_t^s - \tilde{u}_t^s)/\bar{\kappa}_\Theta}\mathrm{d}u_t^s \tag{3.34}$$

where we have also used (3.32) and (3.33). Integrating (3.34) along the path 2–3–4 we finally have the dilation response, namely

$$(u_n^s - \tilde{u}_n^s)/\bar{\kappa}_\Theta = 2(\Phi_s - \Phi)[e^{(u_t^s - \tilde{u}_t^s)/\bar{\kappa}_\Theta} - 1] \tag{3.35}$$

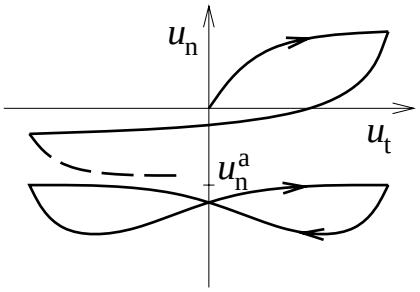

Figure 24: Rotating cone model for granular layer: dilatancy response to cyclic shearing.

where $\tilde{u}_n^s$ is the relative normal displacement at load reversal. The dilatancy and frictional response resulting from the solution (3.33) and (3.35) is depicted in Fig. 23(b).

Let us note that the assumptions adopted in the above example result in contact compaction at each load reversal [$\Delta u_n^s = -2(\Phi_s - \Phi)\bar{\kappa}_\Theta$ between steady sliding states, cf. eqn. (3.35)]. Since this is a non-physical result, we shall no longer assume that the steady state dilation angle Ψ_s is not constant. Instead we assume that there is an asymptotic thickness of the granular layer which depends on the normal pressure. Thus even for the points of the steady state surface some dilation may occur until the asymptotic thickness is not attained. We thus propose the following evolution law for Ψ_s

$$\dot{\Psi}_s = -\left[\frac{u_n^s - u_n^{\rm as}}{\bar{\kappa}_\Psi} + 2\eta\Psi_s\right]\frac{\dot{\kappa}_\Psi}{\bar{\kappa}_\Psi}, \qquad \dot{\kappa}_\Psi = |\dot{u}_t^s| \tag{3.36}$$

where $u_n^{\rm as} = u_n^{\rm as}(t_n)$ is a relative normal displacement related to the asymptotic thickness of the layer and $\bar{\kappa}_\Psi$ is a parameter providing the displacement scale for evolution of Ψ_s. Since in view of (3.30) and (3.32), equation (3.36) is in fact a second order differential equation for $u_n^s(u_t^s)$ we introduce a critical damping term $2\eta\Psi_s$ with $\eta > 1$ in order to avoid oscillatory solutions. The dilatancy response to cyclic shearing is schematically shown in Fig. 24.

Concluding, the model of the third body granular layer involves the yield surface (3.25) and the slip rule (3.28) accompanied by the evolution laws for rotation angle Θ and steady state dilation angle Ψ_c, eqns. (3.30) and (3.36). The parameters of the model are: Φ_s, Φ, $\bar{\kappa}_\Theta$ and $\bar{\kappa}_\Psi$. Also the function $u_n^{\rm as}(t_n)$ must be specified (as a first approximation we may assume $u_n^{\rm as} = 0$).

4 Discussion and conclusions

The friction and dilatancy effects at brittle interfaces have been studied in the paper. As already discussed, the term *brittle interfaces* denotes a wide class of both cohesive and non-cohesive interfaces where the contacting bodies are brittle. This, however, implies another common characteristic feature, namely the wear debris and the material of crushed asperities form a third body layer which can be regarded a granular material. Also, even more importantly, in practice most of the brittle interfaces are characterized by

interlocked asperities and related friction and dilatancy effects. The later effects are crucial for constitutive modelling, especially in the case of non-monotonic and cyclic loading programs.

We have shown, that some of the effects observed in the experiments may result from more than one mechanism. This mostly regards the monotonic response effects, such as peak friction and dilation in direct shear (effects A.3 and A.6 in Table 2). Thus the response to monotonic shearing may not be sufficient to distinguish between the mechanisms and, quite obviously, to predict the non-monotonic or cyclic response.

The most important micro-mechanisms occurring at brittle interfaces have been identified, namely decohesion, interaction of interlocked primary asperities including wear and damage and formation of a third body granular layer. Simple constitutive models have also been proposed providing description of each of these mechanisms separately and through a qualitative analysis the predicting capabilities of the models have been assessed.

The analysis of existing models for cohesive interfaces (Section 3.1) leads to the conclusion that these models are mostly suitable for monotonic loading processes. Particularly, the predictions of cyclic dilation response, cf. Fig. 12(b), are qualitatively different from the typical response types observed in experiments, cf. Fig. 6. The reason is that most of these models neglect the interlocked asperity interaction mode. The model of Giambanco and Di Gati (1997) is an exception as it provides a transition from the cohesive mode to the asperity interaction mode.

In Section 3.2, a model of configurational dilatancy has been proposed. This model generalizes the concepts of interaction of interlocked primary asperities (well-known in the field of rock joints). The model provides a transition from the interlocked to the random asperity contact mode with increasing shearing displacement and describes the related friction and dilatancy effects. A refined model might also include the description of the evolution of elastic stiffness properties of the interface coupled with the transition from the interlocked to the random asperity contact, cf. Fig. 3.

Finally, in Section 3.3, a model for a granular third body layer has been proposed based on the concept of a rotating cone representing rearrangement of the particle configurations associated with shearing in different directions. The model predicts a drop of the dilation angle at each load reversal as well as transient and hysteretic effects.

While the simple models presented in Section 3 apply for specific mechanisms only there is a need for a complete, combined model describing all the related phenomena (decohesion, configurational dilatancy effects, formation and shearing of the third body layer), cf. Fig. 25. The model should couple damage in the process zone occurring during the decohesion process with the formation of a rough interface and, subsequently, wear and damage of asperities with formation of the granular third body layer. Such model will be the subject of future work.

Acknowledgement This work has been supported by the INCO Copernicus programme through the project No ERBIC15CT970706.

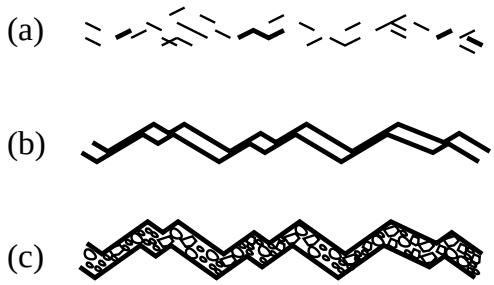

Figure 25: The basic mechanisms occurring at brittle interfaces: (a) decohesion; (b) interaction of interlocked asperities; (c) formation and shearing of the third body layer.

References

[1] A. Anthoine, G. Magenes, and G. Magonette. Shear-compression testing and analysis of brick masonry walls. In G. Duma, editor, *Proc. 10th European Conference on Earthquake Engineering*, volume 3, pages 1657–1662. Balkema, Rotterdam, 1995.

[2] R.H. Atkinson, B.P. Amadei, S. Saeb, and S. Sture. Response of masonry bed joints in direct shear. *J. Struc. Eng., ASCE*, 115(9):2276–2296, 1989.

[3] S. Bandis, A.C. Lumsden, and N.R. Barton. Experimental studies of scale effect on the shear behaviour of rock joints. *Int. J. Rock Mech. Min. Sci. Geomech. Abstr.*, 18:1–21, 1981.

[4] S.C. Bandis, A.C. Lumsden, and N.R. Barton. Fundamentals of rock joint deformation. *Int. J. Rock Mech. Min. Sci. Geomech. Abstr.*, 20:249–268, 1983.

[5] L. Binda, G. Mirabella, C. Tiraboschi, and S. Abbaneo. Measuring masonry material properties. In *Proc. U.S.-Italy Workshop on Guidelines for Seismic Evaluation and Rehabilitation of Unreinforced Masonry Buildings*, pages 6–3/24. State Univ. of New York at Buffalo, NCEER-94-0021, 1994.

[6] D.J. Fox, D.D. Kana, and S.M. Hsiung. Influence of interface roughness on dynamic shear behavior in jointed rock. *Int. J. Rock Mech. Min. Sci.*, 35(7):923–940, 1998.

[7] A. Gajo and D. Muir Wood. A kinematic hardening constitutive model for sands: The multiaxial formulation. *Int. J. Num. Anal. Meth. Geomech.*, 23:925–965, 1999.

[8] L. Gambarotta and S. Lagomarsino. Damage models for the seismic response of brick masonry shear walls. Part I: The mortar joint model and its applications. *Earthquake Engrg. Struct. Dyn.*, 26:441–462, 1997.

[9] A. Gens, I. Carol, and E.E. Alonso. Elasto-plastic model for joints and interfaces. In D.R.J. Owen et al., editor, *Proc. 2nd Int. Conf. Computational Plasticity*, pages 1251–1264, Swansea, UK, 1989. Pineridge Press.

[10] C. Gerrard. Shear failure of rock joints: appropriate constraints for empirical relations. *Int. J. Rock Mech. Min. Sci. Geomech. Abstr.*, 23(6):421–429, 1986.

[11] G. Giambanco and L. Di Gati. A cohesive interface model for the structural mechanics of block masonry. *Mech. Res. Commun.*, 24(5):503–512, 1997.

[12] R.W. Hutson and C.H. Dowding. Joint asperity degradation during cyclic shearing. *Int. J. Rock Mech. Min. Sci. Geomech. Abstr.*, 27(2):109–119, 1990.

[13] J.C. Jaeger. Friction of rocks and stability of rock slopes. *Geotechnique*, 21(2):97–134, 1971.

[14] H.K. Kutter and G. Weissbach. Der Einfluss von Verformungs- und Belastungsgeschichte auf den Scherwiderstand von Gesteinskluften unter besonderer Berucksichtigung der Mylonitbildung. Final Report, DFG Research Project Ku 361/2/4, 1980.

[15] H.R. Lotfi and P.B. Shing. Interface model applied to fracture of masonry structures. *J. Struct. Engrg., ASCE*, 120(1):63–80, 1994.

[16] P.B. Lourenco and J.G. Rots. Multisurface interface model for analysis of masonry structures. *J. Eng. Mech. ASCE*, 123(7):660–668, 1997.

[17] D.B. Marshall and W.C. Oliver. An indentation method for measuring residual stresses in fiber-reinforced ceramics. *Mat. Sci. Engrg. A*, 126:95–103, 1990.

[18] D.B. Marshall, M.C. Shaw, and W.L. Morris. Measurement of interfacial debonding and sliding resistance in fiber reinforced intermetallics. *Acta Metall. Mater.*, 40(3):443–454, 1992.

[19] Z. Mróz and G. Giambanco. An interface model for analysis of deformation behaviour of discontinuities. *Int. J. Num. Anal. Meth. Geomech.*, 20:1–33, 1996.

[20] Z. Mróz and S. Stupkiewicz. An anisotropic friction and wear model. *Int. J. Sol. Struct.*, 31(8):1113–1131, 1994.

[21] Z. Mróz and S. Stupkiewicz. Constitutive model of adhesive and ploughing friction in metal forming processes. *Int. J. Mech. Sci.*, 40:281–303, 1998.

[22] F.D. Patton. *Multiple modes of shear failure in rock and related materials.* PhD thesis, University of Illinois, 1966.

[23] M.E. Plesha. Constitutive models for rock discontinuities with dilatancy and surface degradation. *Int. J. Num. Anal. Meth. Geomech.*, 11:345–362, 1987.

[24] R. van der Pluijm. Shear behaviour of bed joints. In A.A. Hamid and H.G. Harris, editors, *Proc. 6th North American Masonry Conf.*, pages 125–136. Drexel University, Philadelphia, Pennsylvania, USA, 1993.

[25] R. van der Pluijm. Non-linear behavior of masonry under tension. *Heron*, 42(1):25–54, 1997.

[26] M. Raous, L. Cangemi, and M. Cocu. A consistent model coupling adhesion, friction and unilateral contact. *Comp. Meth. Appl. Mech. Engrg.*, 177:383–399, 1999.

[27] M.F. Snyman and J.B. Martin. A consistent formulation of a dilatant interface element. *Int. J. Num. Anal. Meth. Geomech.*, 16:493–527, 1992.

[28] S. Stupkiewicz. Fiber sliding model accounting for interfacial micro-dilatancy. *Mech. Mater.*, 22:65–84, 1996.

[29] Z. Sun, C. Gerrard, and O. Stephanson. Rock joint compliance tests for compression and shear loads. *Int. J. Rock Mech. Min. Sci. Geomech. Abstr.*, 4:197–213, 1985.